An AAV variant enables human T cell engineering *in vivo*

Zhike Lu[1,2,3#], Ke Ni[1,2,3#], Wenjun Liu[4#], Qingkai Song[1,2], Rong Zheng[1,2], Ming Wei[3], Yinling Zhang[2], Jing Wang[1,2], Lina Wei[3], Chenlu Wu[2,3], Qingfeng Zhang[3], Jiamei Wu[3], Shuai Ding[4], Rujie Zhu[4], Chunyu Cheng[4], Yanyi Cong[3], Yinxia Xu[3], Baorui Kong[3], Shanshan Wu[3], Gang Wang[3], Xiaojuan Wang[2], Yalin Wang[2], Xu Qian[5], Ruixia Deng[3], Hui Chen[3], Yan Li[*4,6,7,8], Lijia Ma[*1,2,3,6]

Autologous chimeric antigen receptor T (CAR-T) cell therapy has demonstrated therapeutic effectiveness in hematologic malignancies and autoimmune diseases. However, the manufacturing complexity and the requirement for lymphodepletion have hindered its widespread clinical application. Engineering human T cells *in vivo* holds promise to conquer these limitations but requires effective T cell-targeted CAR delivery with demonstrated safety. Here, we show that an engineered AAV6 variant, AAV6-M2, enables *in vivo* CAR expression in human T cells following systemic administration in a Humanized Immune System (HIS) mouse model. AAV6-M2-CD19CAR turned up to 77.5% of human $CD8^+$ T cells into CAR-T cells across multiple organs six weeks post-AAV injection. In HIS mice exhibiting systemic lupus erythematosus-like symptoms, AAV6-M2-CD19CAR treatment effectively depleted B cells in both peripheral blood and tissues, accompanied by ameliorated lupus pathologies. Importantly, systemic delivery of AAV6-M2 resulted in significant liver de-targeting, with viral genome levels in the liver reduced by over two orders of magnitude in both mice and cynomolgus macaques compared to wild-type AAV. Through CRISPR screening, cryo-EM structural analysis, and molecular docking, we identified CD62L as a key mediator of AAV6-M2's enhanced transduction to human T cells, enabling CAR delivery without the need for prior T cell activation. These findings establish that AAV-mediated CAR delivery can generate functional human CAR-T cells *in vivo*, providing mechanistic insights into the selective targeting of T cells. This work highlights engineered AAV vectors as a promising platform for *in vivo* CAR-T therapy and expands the therapeutic landscape of AAV beyond inherited diseases.

https://doi.org/10.15302/vita.2026.01.0008

INTRODUCTION

Ex vivo chimeric antigen receptor T (CAR-T) cell therapy has shown remarkable success in treating both malignant and autoactivated B cells[1]. This therapy has led to high rates of long-lasting remission in patients with relapsed or refractory cancers or autoimmune diseases who previously had limited treatment options. Despite its success, challenges remain for the current FDA-approved autologous CAR-T therapy, which is personalized and requires the collection of a patient's T cells, genetic modifications to express CARs, and lymphodepletion prior to CAR-T cell infusion[2]. Off-the-shelf CAR-T therapy, also called allogeneic CAR-T, uses T cells from donors or derived from iPSC, providing immediate availability of the CAR-T cell product[1]. However, issues of allogeneic CAR-T include life-threatening graft-versus-host diseases (GvHD) and rapid elimination by the host immune system[3].

In vivo CAR-T cell therapy involves delivering the CAR sequence directly into the patient's T cells within their body. CAR sequence is packed by viral or non-viral delivery platforms, which is also "off-the-shelf" while bypassing the GvHD of allogeneic CAR-T cell therapy. In this context, *in vivo* CAR-T is no longer a personalized cell therapy but a ready-to-use gene therapy. Thus, it faces the same challenge as gene therapy: efficiently and specifically delivering the CAR sequence to T cells. Several delivery platforms have been used to develop *in vivo* CAR-T therapy. Lipid nanoparticles (LNP) packing mRNA-encoding CAR sequence have been conjugated with antibodies, including anti-CD3, CD8, and CD5, to achieve redirection to T cells rather than the liver *in vivo*[4-9]. Although the COVID-19 vaccine has proved the safety and scalability of this platform, antibody-conjugated LNPs face challenges in large-scale manufacturing and unclear long-term clinical safety following intravenous administration. Lentivirus (LV) with an engineered envelope with single-chain variable fragments (scFv) against CD3, CD4, CD7, CD8, or TCR could also be redirected to T cells *in vivo*[10-16]. LV integrates the CAR sequence into the host cell genome, allowing stable transgene expression through T-cell expansion while also raising safety concerns on sequence integration into the genome of bystander cells and insertional mutagenesis. Virus-like particles (VLPs) resemble viruses but lack viral genetic material, making them non-infectious[17,18]. VLP allows *in vivo* delivery of Ribonucleoprotein (RNP) instead of DNA. A recent study engineered VLP by pairing the display of a mutated VSVG with

1. Westlake Laboratory, Hangzhou, Zhejiang, China. 2. School of Life Sciences, CryoEM Core Facility, Westlake University, Hangzhou, Zhejiang, China. 3. Westlake Genetech, Hangzhou, Zhejiang, China. 4. MOE Key Laboratory of Model Animal for Disease Study, Model Animal Research Center, Department of Rheumatology and Immunology, Nanjing Drum Tower Hospital, The Affiliated Hospital of Medical School, Nanjing University, Nanjing, Jiangsu, China. 5. Department of Clinical Laboratory, Zhejiang Cancer Hospital, Hangzhou Institute of Medicine, Chinese Academy of Sciences, Hangzhou, Zhejiang, China. 6. Changping Laboratory, Beijing, China. 7. ChemBioMed Interdisciplinary Research Center at Nanjing University, Nanjing, Jiangsu, China. 8. Wuxi Xishan NJU Institute of Applied Biotechnology, Wuxi, Jiangsu, China. #These authors contributed equally. *Correspondence: Yan Li (yanli@nju.edu.cn), Lijia Ma (ma.lijia@outlook.com)
Received: December 19, 2025; Accepted: January 31, 2026; Published: February 3, 2026

anti-CD3, CD4, or CD28 scFv on Cas9-EDVs (enveloped delivery vehicles) to target T cells *in vivo* and deliver genome editor and CAR sequences[19]. Although the concept is well-established, the less efficient generation of CAR-T cells *in vivo* and the complicated manufacturing process limit their applications in clinics.

Recombinant AAV vectors (AAVs) have been widely used in gene therapy due to their safety profile and ability to induce long-term expression of transgenes in non-dividing cells. Although wild-type (WT) AAVs naturally accumulate in the liver by systemic injection, engineering the variable regions of the capsid protein of AAV has proved to be effective in redirecting AAV to extrahepatic organs or tissues (e.g., the central nervous system and muscle) or increasing transduction efficiencies to non-hepatic cells[20]. For example, DART-AAV inserted a designed ankyrin repeat protein (DARPin) targeting murine CD8 into the GH2-GH3 loop of AAV2 capsid protein VP1 and resulted in over 20-fold increase in transduction activity in murine T cells compared to AAV2[10]. Ark313 is an AAV6 variant targeting murine T cells, which was engineered through three rounds of directed evolution of a capsid library with 7-mer random insertion in the variable region IV[21]. Infusion of Ark313-generated CAR-T cells demonstrated better efficacy in controlling tumor growth than retrovirus-generated CAR-T cells. In a follow-up study, intravenous Ark313 injection successfully transduced murine T cells in vivo[22]. However, the question of whether an engineered AAV variant could enable the *in vivo* targeting of human T cells, while staying away from the liver and other organs, through systemic delivery, has yet to be explored.

Here, we demonstrated that an engineered AAV6 variant, AAV6-M2, could effectively engineer human T cells both *in vitro* and *in vivo*. *In vitro*, AAV6-M2 successfully delivered the CD19 CAR sequence into both activated and resting human T cells, leading to robust, antigen-dependent cytotoxicity. Further, evidence from whole-genome CRISPR screening, targeted gene knockout, cryo-electron microscopy (cryo-EM) structural analysis, and molecular docking collectively underscores the critical role of CD62L, a cell surface marker of less-differentiated T cells[23], in facilitating AAV6-M2 transduction into resting T cells without prior activation. Systemic administration of AAV6-M2-CAR into Humanized Immune System (HIS) mice resulted in the generation of up to 77.5% of $CD8^+$ CAR-T cells six weeks post AAV injection. In the HIS mice with systemic lupus erythematosus (SLE), this approach successfully ameliorated lupus pathologies, correlating with the depletion of both circulating and tissue-resident B cells. Notably, systemic injection of AAV6-M2 led to approximately two orders of magnitude lower liver accumulation compared to WT AAV, in both mice and cynomolgus macaques, highlighting a favorable safety profile. Collectively, this study positions AAV6-M2 as a clinically translatable vector for *in vivo* CAR-T therapy and broadens the therapeutic scope of AAV-based gene delivery from inherited disorders to autoimmune diseases.

RESULTS

AAV6 variants show superior transduction efficiencies in human primary T cells

To design a capsid library with an improved likelihood of identifying variants with specific tropism for human T cells, we collected functional peptides reported from publicly available databases and literature. For these peptide sequences, we randomly selected fragments with 6–12 amino acids and inserted them between residues A581 and T593 of the AAV6 capsid protein VP3 (variable region VIII or VR VIII)[24], yielding a diverse library comprising ~480,000 AAV6 variants. Following capsid library screening in human primary T cells, we identified variants that exhibited enhanced transduction efficiencies relative to WT AAV6 (AAV6-WT). Among them, two top-performing candidates, designated AAV6-M1 and AAV6-M2, were selected based on their transduction efficiencies and low coefficient of variation in transduction performance across replicates (Supplementary Fig. S1a).

To validate the transduction efficiencies of the leading candidates in human primary T cells, we packaged self-complementary AAVs encoding EGFP using the AAV6-M1 and AAV6-M2 capsids and compared their performance to AAV6-WT (Fig. 1a). Transduction efficiency was quantified by counting the percentage of $EGFP^+$ T cells. Across a range of multiplicities of infection (MOI: 1×10^2, 1×10^3, and 1×10^4), both AAV6-M variants outperformed AAV6-WT (Fig. 1b). This superiority was consistent when assessing both the percentage of $EGFP^+$ cells and the mean fluorescent intensity (MFI) (Fig. 1c, d). Notably, at an MOI of 1×10^3, the AAV6-M1 and AAV6-M2 achieved $EGFP^+$ rates of 91.8% and 80.2%, respectively — matching or exceeding the transduction efficiency observed with AAV6-WT at an MOI one order of magnitude higher (1×10^4). Moreover, the engineered AAV6-M2 exhibited packaging efficiency comparable to that of AAV6-WT, whereas AAV6-M1 showed a reduced packaging yield (Supplementary Fig. S1b). The manufacturability of AAV6-M2 was further verified in a scaled-up 3-liter bioreactor, demonstrating comparable packaging efficiency to AAV6-WT, a dominant full-particle peak, and uniform capsid morphology (Supplementary Fig. S1c–e).

CD62L mediates enhanced transduction of AAV6-M2 in human T cells

AAV6-M variants were assembled using engineered capsid proteins containing mutations between residues A581 and T593 of VP3, where the corresponding peptides are located in the 3-fold protrusion of AAV particles and are positioned to interact directly with host cells. We hypothesized that these variants utilized distinct cell-surface factors to enter human T cells, compared to AAV6-WT. To investigate this, we performed a whole-genome CRISPR knockout screen in Jurkat cells to identify genes contributing to the enhanced transduction efficiencies of AAV6-M variants (Fig. 2a). In brief, Jurkat cells stably expressing SpCas9 (Jurkat-Cas9) were first transduced with the lentiviral CRISPR Brunello library at a low MOI to deliver one sgRNA per cell, followed by transduction with either AAV6-WT-EGFP, AAV6-M1-EGFP, or AAV6-M2-EGFP. We then sorted and collected the top and bottom 20% Jurkat-Cas9 cells according to EGFP expression. Compared to the top 20%, sgRNAs enriched in the bottom 20% of cells represented gene knockouts that disrupted the AAV attachment, internalization, or intracellular trafficking in human T cells.

We analyzed the top 10 genes enriched in each of the three CRISPR screens. All screens identified genes that are known to be essential for AAV transduction and trafficking, including *KIAA0319L* (*AAVR*) and *TM9SF2*, validating the effectiveness of our screening approach. A few genes, such as *NOTCH1*, were specifically enriched in the screen using AAV6-M1 relative to AAV6-WT (Supplementary Fig. S2a). However, NOTCH1 is broadly expressed across multiple organs, including

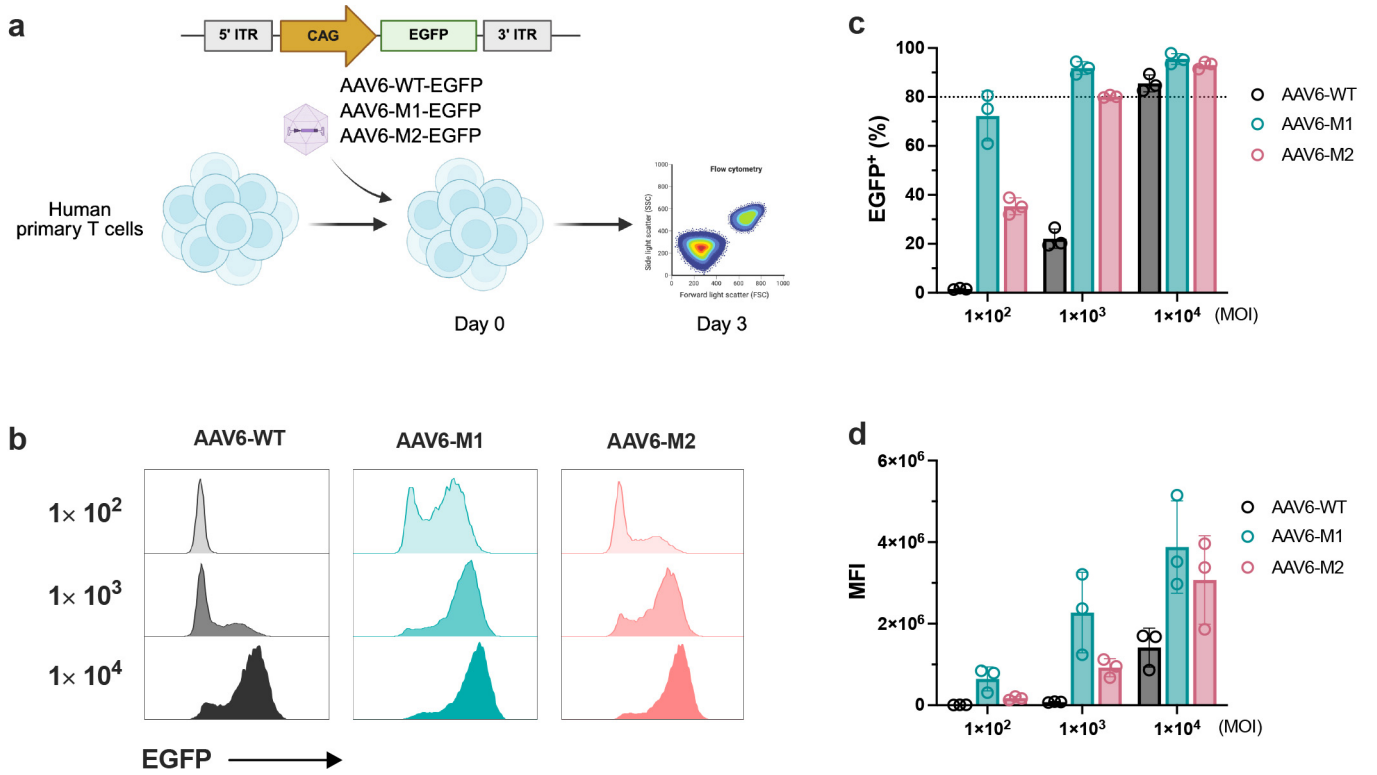

Fig. 1 AAV6 variants show superior transduction efficiencies in human primary T cells. a A schema of scAAV6-EGFP transduction in human primary T cells. **b–d** The transduction efficiency was illustrated in a fluorescence histogram (**b**), percentage of EGFP$^+$ cells (**c**), and MFI (**d**).

endocrine tissues, brain, and liver, making it less favorable for selective *in vivo* T-cell targeting. Nevertheless, among the top 10 genes specifically enriched in the AAV6-M2 screen, *SELL* stood out (Fig. 2b, c). *SELL* encodes a cell surface protein and is almost exclusively expressed in immune cells. Also known as CD62L or L-selectin, SELL is essential for the binding and rolling of lymphocytes on endothelial cells, facilitating their migration into secondary lymphoid organs. Interestingly, a recent study engineered lentiviral envelopes with CD62L-specific scFv to enable CAR delivery into less differentiated human T cells[25].

Indeed, knocking out *CD62L* (*SELL*) from Jurkat cells significantly reduced the transduction efficiency of AAV6-M2 but not AAV6-WT (Fig. 2d). The reduction was comparable to that observed upon *AAVR* knockout, suggesting a critical and specific role of CD62L in mediating AAV6-M2 entry into T cells. Moreover, we used two independent sgRNAs to knock out *CD62L* in primary human T cells from three donors. Following *CD62L* knockout, the transduction efficiency of AAV6-M2 was markedly diminished, while AAV6-WT transduction remained largely unaffected (Fig.2e; Supplementary Fig. S2b). Accordingly, overexpression of CD62L in CD62L-negative cells enhanced AAV6-M2 binding (Supplementary Fig. S2c). Collectively, both CRISPR screening, targeted gene knockout, and CD62L overexpression experiments underscore the essential role of CD62L in AAV6-M2 transduction into human T cells — a mechanism that appears unique to this AAV variant and is not shared by AAV6-WT.

To further investigate how the engineered loop may enhance the interaction between AAV6-M2 and CD62L, we resolved the cryo-EM structure of AAV6-M2 at 1.8 Å resolution (PDB: 9VI4; Fig. 2f; Supplementary Fig. S2d). The VP protein monomer was accurately modeled, with both the backbone and side chains in the VR VIII loop clearly resolved (Supplementary Fig. S2e). Structural alignment showed that the backbone conformation of AAV6-M2 was nearly identical to that of AAV6-WT (PDB: 4V86) (Supplementary Fig. S2f); however, the side chain conformations within the VR VIII loop differ substantially (Supplementary Fig. S2g, h). To explore potential interactions with CD62L, we performed molecular docking between AAV6-M2 and human CD62L (PDB: 5VC1; lectin/EGF domains). The engineered loop was predicted to insert into the EGF domain of CD62L, where three negatively-charged residues (E590, E591, and E592) within the VR VIII loop of AAV6-M2 engage a positively-charged surface pocket through electrostatic interactions (Figs. 2g, h). Mutating each one of these glutamic acids individually, or all of them collectively, to alanine abolished the binding affinity between AAV6-M2 and human T cells, further highlighting the critical roles of these residues (Supplementary Fig. S2i). These structural observations suggest that the engineered VR VIII loop appears to contribute to enhancing the engagement between AAV6-M2 and CD62L. The engineered loop, however, did not increase but slightly reduced neutralization by human serum compared to AAV6-WT (Fig. 2i; Supplementary Fig. S2j).

AAV6-M2 transduces resting human T cells *in vitro*

Considering both the efficiencies of viral packaging and the specificity of the binding partner, we focused on AAV6-M2 in the subsequent studies. We first replaced the transgene with CD19 CAR to evaluate the expression kinetics and cytotoxicity of AAV6-M2-mediated CAR-T cells *in vitro* (Supplementary Fig. S3a). Following transduction of bead-activated human T cells (aT) with AAV6-M2-CAR, the proportion of CAR$^+$ T cells peaked at day 3 and gradually declined by day 10 (Fig. 3a). We observed comparable T cell viability and proliferation relative to the non-AAV control (Fig. 3b; Supplementary Fig. S3b). When co-cultured with CD19-expressing NALM6 cells, AAV6-M2-transduced T cells exhibited robust cytotoxicity by 20 h post-transduction and achieved complete B cell killing by

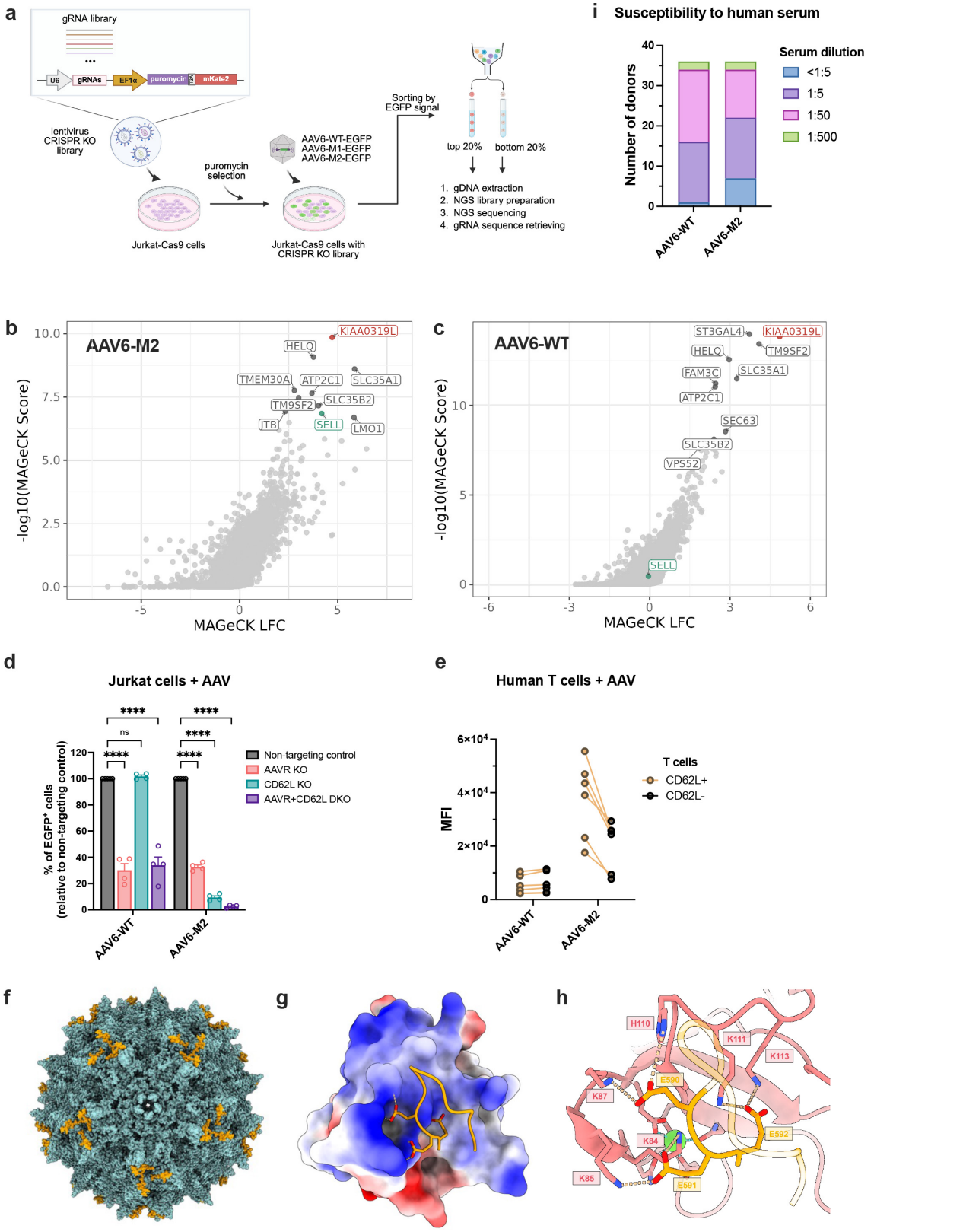

Fig. 2 CD62L mediates enhanced transduction of AAV6-M2 in human T cells. a Schematic of the CRISPR screening strategy. **b, c** Volcano plots of genome-wide CRISPR screen hits for AAV6-M2 (**b**) and AAV6-WT (**c**), showing MAGeCK score vs log-fold change (LFC). Top-ranked candidates, including *SELL*, are highlighted. **d** EGFP expression in Jurkat cells transduced with AAV6-M2 or AAV6-WT following *AAVR* knockout, *CD62L* knockout (two independent sgRNAs), or *AAVR+CD62L* double knockout. CD62L-negative cells were sorted in the analysis of *CD62L* knockout and *AAVR+CD62L* double knockout groups. **e** Flow cytometry analysis of MFI of EGFP in $CD62L^+$ and $CD62L^-$ human primary T cells transduced with AAV6-M2 and AAV6-WT. Data collected from T cells of three donors and *CD62L*-knockout by two independent sgRNAs. **f** Surface representation of the AAV6-M2 capsid resolved at 1.8 Å resolution by cryo-EM. The engineered VR VIII loops are highlighted in yellow. **g** Electrostatic surface potential map of the CD62L EGF domain (PDB: 5VC1), with the engineered VR VIII loop of AAV6-M2 (yellow, PDB: 9VI4) docked into the binding pocket. **h** Detailed view of the docking interface between the engineered VR VIII loop (yellow) and CD62L EGF domain (pink), showing residue-level interactions, including hydrogen bonds (dotted lines). **i** Bar graph showing the distribution of the highest serum dilution titer against AAV6-WT and AAV6-M2 in human serum from 36 donors. Serum susceptibility is grouped by the highest dilution factor at which EGFP expression dropped below 50%. Data shown as mean ± SEM. *P* values (**d**) were calculated by two-way ANOVA. ns: not significant; ****$P \leq 0.0001$.

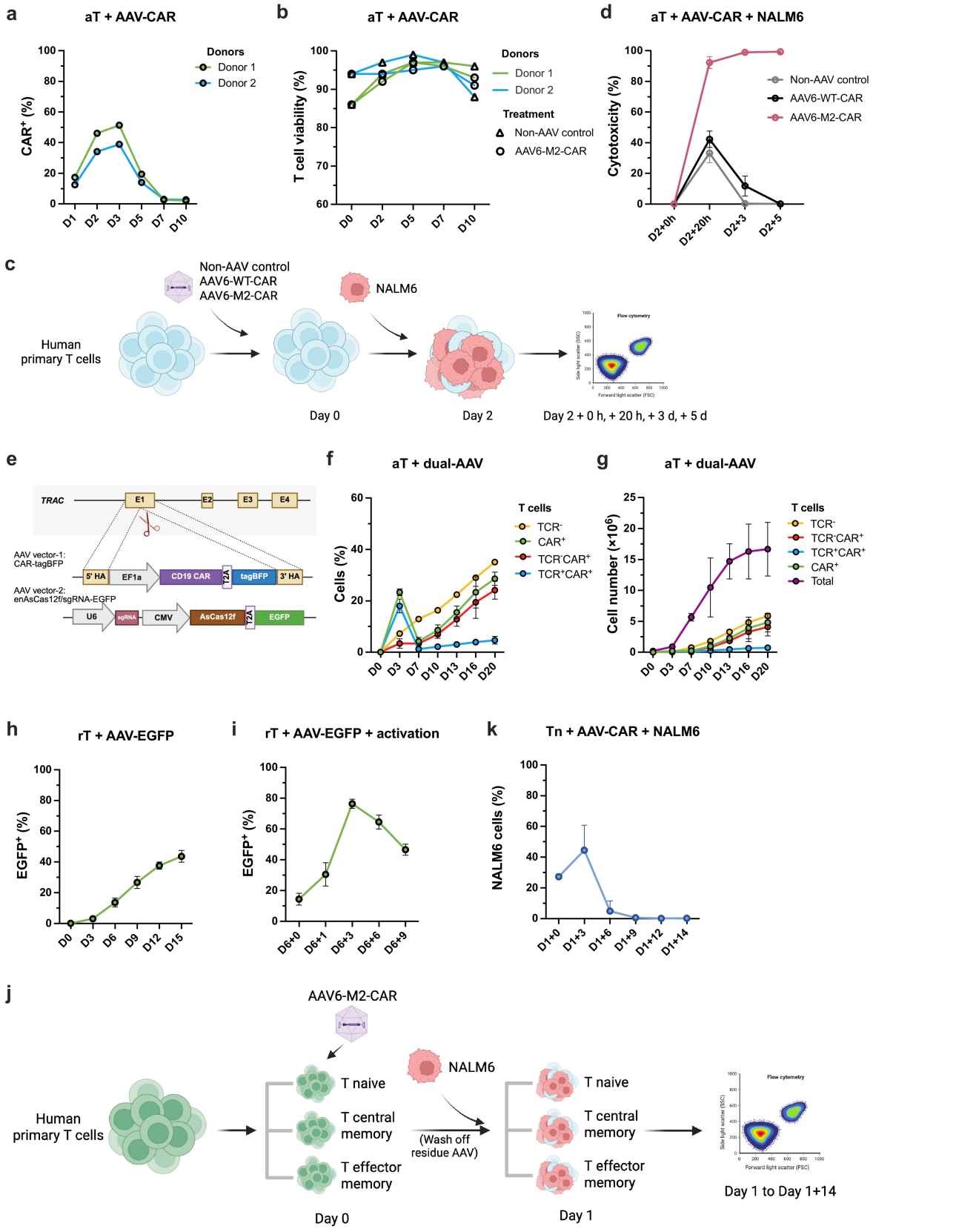

Fig. 3 Efficient transduction and cytotoxicity of AAV6-M2-mediated CAR delivery in human T cells. a Time course of CAR expression in activated T cells (aT) from two donors after AAV6-M2-CAR transduction (MOI = 5E4), measured by flow cytometry. **b** Viability of aT cells after AAV6-M2-CAR transduction, compared to non-AAV controls. **c** Schematic of the cytotoxicity assay setup, showing transduction, co-culture with NALM6 cells, and flow cytometry-based quantification of target cell killing. **d** Cytotoxicity assay of AAV-CAR-transduced aT cells (MOI = 1E 4) co-cultured with NALM6 cells (T:B = 1:1). Cytotoxicity was assessed at multiple time points post co-culture. **e** Construct design of the dual-AAV knock-in strategy targeting the *TRAC* locus: AAV vector-1 delivers the CAR-tagBFP cassette flanked by homology arms, and AAV vector-2 expresses sgRNA, enAsCas12f, and EGFP. **f**, **g** Quantification of cell populations over time by percentage (**f**) or cell numbers (**g**) after dual-AAV delivery in aT cells. **h** Time course of EGFP expression in resting T cells (rT) transduced with AAV6-M2-EGFP, measured by flow cytometry. **i** EGFP expression in rT cells post AAV6-M2 transduction followed by activation (Day 6). **j** Experimental design for subtype-specific cytotoxicity assays. Human T cells were sorted into Tn, TCM, and TEM subsets, transduced with AAV6-M2-CAR, and co-cultured with NALM6 cells. **k** NALM6 cell abundance measured by flow cytometry over time following co-culture with Tn cells transduced with AAV6-M2-CAR.

day 3 (Fig. 3c, d; Supplementary Fig. S3c). In contrast, AAV6-WT-transduced T cells showed minimal cytotoxicity. These results demonstrate that AAV6-M2 effectively delivers CD19 CAR to active human T cells, enabling antigen-specific cytotoxicity *in vitro*.

Next, we performed site-specific CD19 CAR insertion using two AAV6-M2 vectors to generate stable CAR-expressing T cells, a strategy expected to prolong CAR-T presence during T cell proliferation. The AAV vector-1 provides the CD19 CAR expression cassette, which is integrated into the 1st exon of *TRAC*, where the AAV vector-2 generates a double-strand break by enAsCas12f-mediated cleavage (Fig. 3e). Following dual AAV transduction, transient CAR^+ T cells (TCR^+CAR^+) emerged rapidly but declined after day 3 (Fig. 3f), coinciding with the onset of robust T-cell expansion (Fig. 3g). In contrast, stable CAR^+ T cells (TCR^-CAR^+) gradually increased over time, expanding in parallel with the proliferating T cell population and exhibiting sustained CAR expression. Together, these results demonstrate that AAV6-M2 enables efficient generation of stable CAR^+ T cells through precise genomic integration of the CAR cassette, thereby supporting prolonged CAR-T expression during T-cell proliferation.

However, since the majority of human T cells are in a resting state *in vivo*, we sought to evaluate the delivery capability of AAV6-M2 in non-activated T cells. In two parallel experiments, non-activated human T cells were transduced with AAV6-M2-EGFP and subsequently either activated or left unstimulated (Supplementary Fig. S3d, e). We then monitored the EGFP expression over time. Interestingly, in the absence of activation, the percentage of $EGFP^+$ cells gradually increased, reaching ~40% by day 15 (Fig. 3h). In contrast, post-transduction activation rapidly elevated the percentage of $EGFP^+$ cells to ~80% within three days, followed by a decline to levels similar to those observed in non-activated cells by the endpoint of the experiment (Fig. 3i). Adding AAV6-M2-EGFP into non-activated human peripheral blood mononuclear cells (PBMC) also showed successful transduction in both $CD4^+$ and $CD8^+$ T cells (Supplementary Fig. S3f). These results indicate that AAV6-M2 is capable of delivering a transgene into human T cells without the need for prior or subsequent activation.

To investigate the antigen-specific cytotoxic potential of core circulating T cell subsets following AAV6-M2-CAR transduction, we co-cultured naïve (Tn), central memory (TCM), and effector memory (TEM) T cells with NALM6 cells (Fig. 3j). In the absence of bead-based activation, Tn cells effectively eliminated NALM6 cells between days 6 and 9 post-co-culture, with some variability observed among donors (Fig. 3k). The cytotoxic activities of TCM and TEM were more variable, with two donors exhibiting complete NALM6 clearance between days 6 and 14 (Supplementary Fig. S3g, h). Upon antigen stimulation, both Tn and TCM underwent phenotypic conversion into TEM (Supplementary Fig. S3i–k). Collectively, AAV6-M2 enables effective CAR delivery to multiple resting T cell subsets and supports their differentiation into functional effectors capable of eliminating target cells in an antigen-dependent manner.

AAV6-M2 mediates *in vivo* CAR-T cell generation and B cell depletion

The AAV-mediated CAR-T cell generation encouraged us to explore the *in vivo* application of AAV6-M2. We are curious whether the superior transduction efficiency of AAV6-M2 to human T cells could enable the generation of CAR-T cells *in vivo* through systemic administration to bypass the *ex vivo* manufacturing process of the conventional CAR-T cell therapy. We employed an optimized HIS mouse model (NCG-X-hIL15), in which human hematopoietic stem cells (hHSCs) were engrafted into immunodeficient mice and various human immune subsets were developed (Fig. 4a). Following engraftment, the HIS mice with comparable levels of human T and B cells were randomly grouped (Supplementary Fig. S4a, b) and systemically injected with AAV6-WT or AAV6-M2 at a dose of 3×10^{13} vg/kg and sacrificed after 28 or 42 days. The same CD19 CAR-EGFP construct used in the *in vitro* assay was applied in the *in vivo* experiment.

In peripheral blood, CAR^+ T cells emerged by week 2 following AAV6-M2-CAR injection, whereas very few CAR^+ T cells were detected in the AAV6-WT-CAR group (Fig. 4b). These CAR^+ cells were predominantly $CD8^+$, with minimal $CD4^+CAR^+$ T cells detected (Fig. 4c). Concurrently, human B cells, the targeted cells of these CAR^+ T cells, decreased over time. The AAV6-M2-CAR group showed a notable decline from baseline to week 4, with B cell counts in most mice approaching the detection threshold (Supplementary Fig. S4c, d). While B cell levels were variable at baseline and across individual mice, the overall trend indicated a greater extent of reduction in the AAV6-M2-CAR group by the study endpoint, compared to the AAV6-WT-CAR group.

In bone marrow, spleen, liver, and lung, the human B cells were largely undetectable in AAV6-M2-treated mice, whereas significantly more B cells remained in mice treated with AAV6-WT (Fig. 4d). Correspondingly, CAR^+ T cells were readily detected in these organs in the AAV6-M2-CAR group, but were largely absent in the AAV6-WT-CAR group (Fig. 4e). Mirroring the observation from the peripheral blood, CAR^+ T cells were predominantly $CD8^+$, with up to 77.5% CAR^+CD8^+ present in the bone marrow at week 6 (Fig. 4f; Supplementary Fig. S4e). Collectively, AAV6-M2 successfully delivered CD19 CAR into the human T cells *in vivo*, which could be detected in the peripheral blood two weeks post-AAV injection, and effectively depleted both circulating and tissue-resident B cells.

To assess the differentiation state within CAR^+CD8^+ T cells *in vivo*, we analyzed Tn, TCM, TEM cells, and terminally differentiated effector memory re-expressing CD45RA (TEMRA) subsets across tissues. CAR^+CD8^+ T cells were predominantly of TEM phenotype, while Tn and TCM subsets were minimally detected in these tissues (Fig. 4g; Supplementary Fig. S4f–i). Given our *in vitro* data showing that Tn and TCM cells adopt a TEM phenotype following AAV-CAR transduction and antigen encounter (Supplementary Fig. S3i–k), the tissue-resident TEM cells observed *in vivo* are likely derived from these early-stage subsets and reflect the active killing of human B cells. Together, these findings suggest that the effective B cell depletion in the AAV6-M2-CAR group is accompanied by a dominant presence of CAR^+CD8^+ TEM cells.

Next, we examined the transduction specificity of AAV6-M2 *in vivo*. Among various immune cell types in tissues and blood, $CD8^+$ T cells were preferentially converted to CAR-T cells compared to $CD4^+$ T cells. CAR^+ cells were barely found in B cells, monocytes, and NK cells (Fig. 4h). As systemically injected AAV tends to accumulate in the liver, we also examined the biodistribution of the AAV vector. Compared to the AAV6-WT, the engineered AAV6-M2 shows significant de-targeting from the liver and reduced viral accumulation

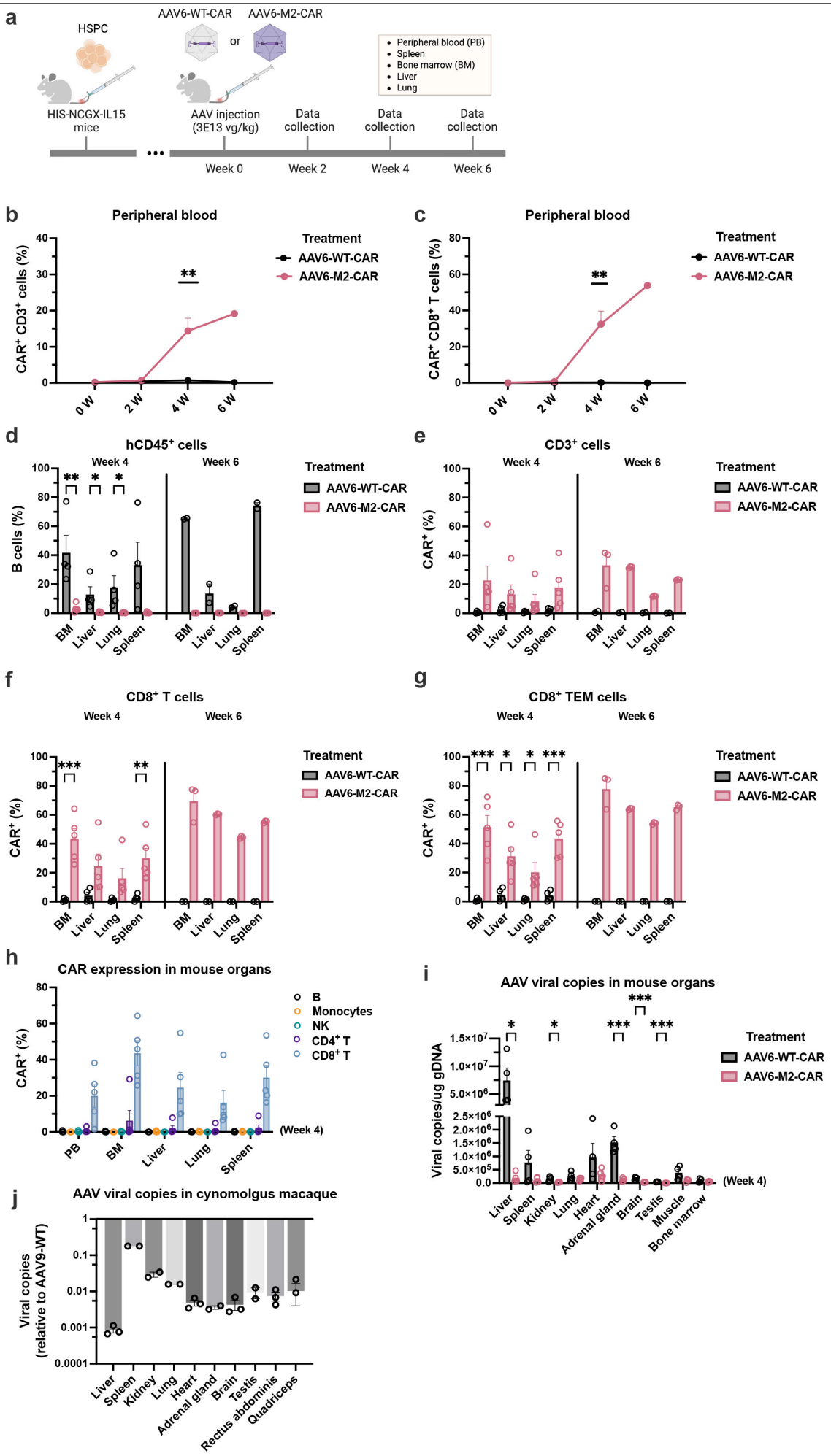
a
HSPC
AAV6-WT-CAR
AAV6-M2-CAR
or
HIS-NCGX-IL15 mice
AAV injection (3E13 vg/kg)
Data collection
Data collection
Data collection
Peripheral blood (PB)
Spleen
Bone marrow (BM)
Liver
Lung
Week 0
Week 2
Week 4
Week 6
b
Peripheral blood
CAR+ CD3+ cells (%)
Treatment
AAV6-WT-CAR
AAV6-M2-CAR
0 W
2 W
4 W
6 W
c
Peripheral blood
CAR+ CD8+ T cells (%)
d
hCD45+ cells
B cells (%)
Week 4
Week 6
BM
Liver
Lung
Spleen
e
CD3+ cells
CAR+ (%)
f
CD8+ T cells
g
CD8+ TEM cells
h
CAR expression in mouse organs
B
Monocytes
NK
CD4+ T
CD8+ T
PB
(Week 4)
i
AAV viral copies in mouse organs
Viral copies/ug gDNA
Kidney
Heart
Adrenal gland
Brain
Testis
Muscle
Bone marrow
j
AAV viral copies in cynomolgus macaque
Viral copies (relative to AAV9-WT)
Rectus abdominis
Quadriceps

Fig. 4 ***In vivo*** **CAR-T cell generation and B cell depletion by AAV6-M2 in humanized mice. a** Schematic of the experimental timeline: HIS-NCGX-IL15 mice were intravenously injected with AAV6-WT-CAR or AAV6-M2-CAR (3×10^{13} vg/kg) and analyzed at 2, 4, and 6 weeks post-injection. **b**, **c** Flow cytometry analysis of CAR^+CD3^+ (**b**) and CAR^+CD8^+ (**c**) T cells in peripheral blood. **d** Percentage of human B cells in various tissues following the administration of AAV6-WT-CAR or AAV6-M2-CAR. **e**–**g** Tissue distribution of CAR^+ cells in $CD3^+$ (**e**), $CD8^+$ (**f**), and $CD8^+$ TEM (**g**) cells. **h** Cellular phenotyping of CAR^+ immune cells across tissues in AAV6-M2-CAR-treated mice. **i** Biodistribution of vector genome copies in mouse organs quantified by qPCR. **j** Relative vector genome copies in cynomolgus macaque organs quantified by NGS. Each dot represents an independent DNA extraction followed by NGS quantification from an individual tissue sample. Each dot represents an animal. Data shown as mean ± SEM. *P* values were calculated by unpaired *t*-tests. Statistical significance levels were not calculated for data in week 6 due to the limited available data points. $^*P \le 0.05$; $^{**}P \le 0.01$; $^{***}P \le 0.001$; $^{****}P \le 0.0001$.

across all organs (Fig. 4i). Furthermore, in cynomolgus macaques, AAV6-M2 showed minimal biodistribution to peripheral tissues, with very low levels of viral genomes detected, including in the liver (Fig. 4j). Together, these findings demonstrate that AAV6-M2 selectively targets human T cells while minimizing off-target liver transduction in both humanized mice and non-human primates, supporting its favorable safety profile for *in vivo* T cell engineering.

AAV6-M2 ameliorated lupus pathologies in SLE HIS mice via B cell depletion

To further evaluate the efficacy of *in vivo* generated CAR-T cells in a disease context, we employed a SLE HIS mouse model induced by topical application of R848, a TLR7/8 agonist (Fig. 5a). SLE HIS mice were randomly assigned to SLE and SLE+AAV groups, with comparable levels of human CD45 cells, human B cells, IgG, and anti-dsDNA antibody (Supplementary Fig. S5a–d). Following systemic administration of AAV6-M2-CAR at week 0, we monitored the B-cell levels in peripheral blood from week 2 to week 8. A rapid and sustained decline in circulating B cells was observed in the SLE+AAV group beginning at week 2, with significantly lower B cell levels compared to the untreated SLE group (Fig. 5b).

To evaluate the tissue-wide impact of CAR-T activity beyond peripheral blood, we quantified human B cells across multiple organs at the study endpoint. Flow cytometry revealed a significant reduction in the percentages of human B cells in the spleen, bone marrow, liver, lung, and kidney of the SLE+AAV group compared to the untreated SLE group (Supplementary Fig. S5e). Although the percentages of B cell reduction in the bone marrow did not reach statistical significance due to an outlier, a clear downward trend was observed, with significantly lower B cell counts detected in the AAV6-M2-treated animals (Fig. 5c). Subtype analysis further demonstrated that the depletion encompassed all major B cell subsets, including transitional, naïve, memory B cells, and plasmablast cells (Supplementary Fig. S5f). Notably, transitional B cells, which represent the majority of developing human B cells in bone marrow, were nearly undetectable following AAV6-M2-CAR administration (Supplementary Fig. S5g). Naïve and memory B cells and plasmablast cells were also significantly reduced in the bone marrow (Supplementary Fig. S5h–j). In the spleen, we found a similar B cell count depletion (Fig. 5d) and a marked reduction of splenic plasmablast and plasma cells (PB&PC), as evidenced by a significant drop in $CD38^+CD138^+$ populations (Supplementary Fig. S5k, l), which are the primary source of autoantibody production in SLE and contribute directly to immune complex deposition and tissue inflammation. Together, bone marrow and spleen analysis inform the direct on-target activity of CAR-T therapy, indicating systemic suppression of B cell development and differentiation.

Lupus nephritis is a major SLE complication associated with progression to renal failure and an overall worse prognosis. In the kidney, the reduction of glomerular IgG deposition in the SLE+AAV group indicated a marked alleviation of immune complex-mediated damage and served as a critical readout for therapeutic efficacy (Fig. 5e; Supplementary Fig. S5m). Consistent with this, circulating levels of anti-dsDNA and anti-Smith (Sm) antibodies significantly declined following AAV treatment (Fig. 5f, g), and serum blood urea nitrogen (BUN) and creatinine (CREA) levels also significantly reduced, indicating improved renal function (Fig. 5h, i). In the lung, histological analysis by hematoxylin and eosin (H&E) staining showed preserved alveolar architecture and reduced inflammatory infiltration in the SLE+AAV group, in contrast to the mild to moderate perivascular and interstitial inflammatory infiltrates observed in the SLE group (Fig. 5j; Supplementary Fig. S5o). Flow cytometry confirmed the depletion of human B cells in the lung, consistent with the observed histological improvement (Supplementary Fig. S5n). In the liver, mild immune cell infiltration was present in the SLE group but completely absent in the SLE+AAV group, aligning with the efficient clearance of tissue-resident B cells (Supplementary Fig. S5p, q). Together, these data demonstrate that administering AAV6-M2-CAR not only eliminates systemic and tissue-resident B cells but also alleviates multi-organ inflammation and protects organ function in a humanized SLE model.

DISCUSSION

This study demonstrates that a clinically validated delivery platform, the recombinant AAV vector, can be engineered to efficiently and specifically deliver transgenes into human T cells both *in vitro* and *in vivo*. We showed that AAV6-M2, an engineered AAV6 variant, successfully generates both transient and stable CAR-expressing T cells *in vitro*. Through a combination of CRISPR screening, cryo-EM, and molecular docking, we identified CD62L, a surface marker expressed on less-differentiated T cells, as a key facilitator of AAV6-M2, but not AAV6-WT, entry into human T cells. This unique tropism enables AAV6-M2 to deliver CD19 CAR into resting human T cells and trigger antigen-dependent cytotoxicity upon encountering $CD19^+$ NALM6 cells. *In vivo*, systemic administration of AAV6-M2-CAR into HIS mice resulted in up to 77.5% of CAR^+CD8^+ T cells six weeks post-injection. In HIS SLE mice, human B cells were effectively depleted in both the peripheral blood and organs, accompanied by improvements in lupus-associated pathologies. Notably, AAV6-M2 exhibited striking liver detargeting, with viral genome accumulation in the liver reduced by more than two orders of magnitude in both mouse and cynomolgus macaque, compared to the WT AAV6 and AAV9.

While LV, LNP, and VLP have been explored for *in vivo* T cell engineering, this study is, to our knowledge, the first to demonstrate that systemic injection of a single AAV vector can generate persistent and functional human CAR-T cells *in vivo*. Given that AAV is used in eight FDA-approved gene therapies, this finding marks an advance in the application of AAV vector for *in vivo* T cell engineering. Natural AAVs are known to accumulate in the liver following intravenous injection.

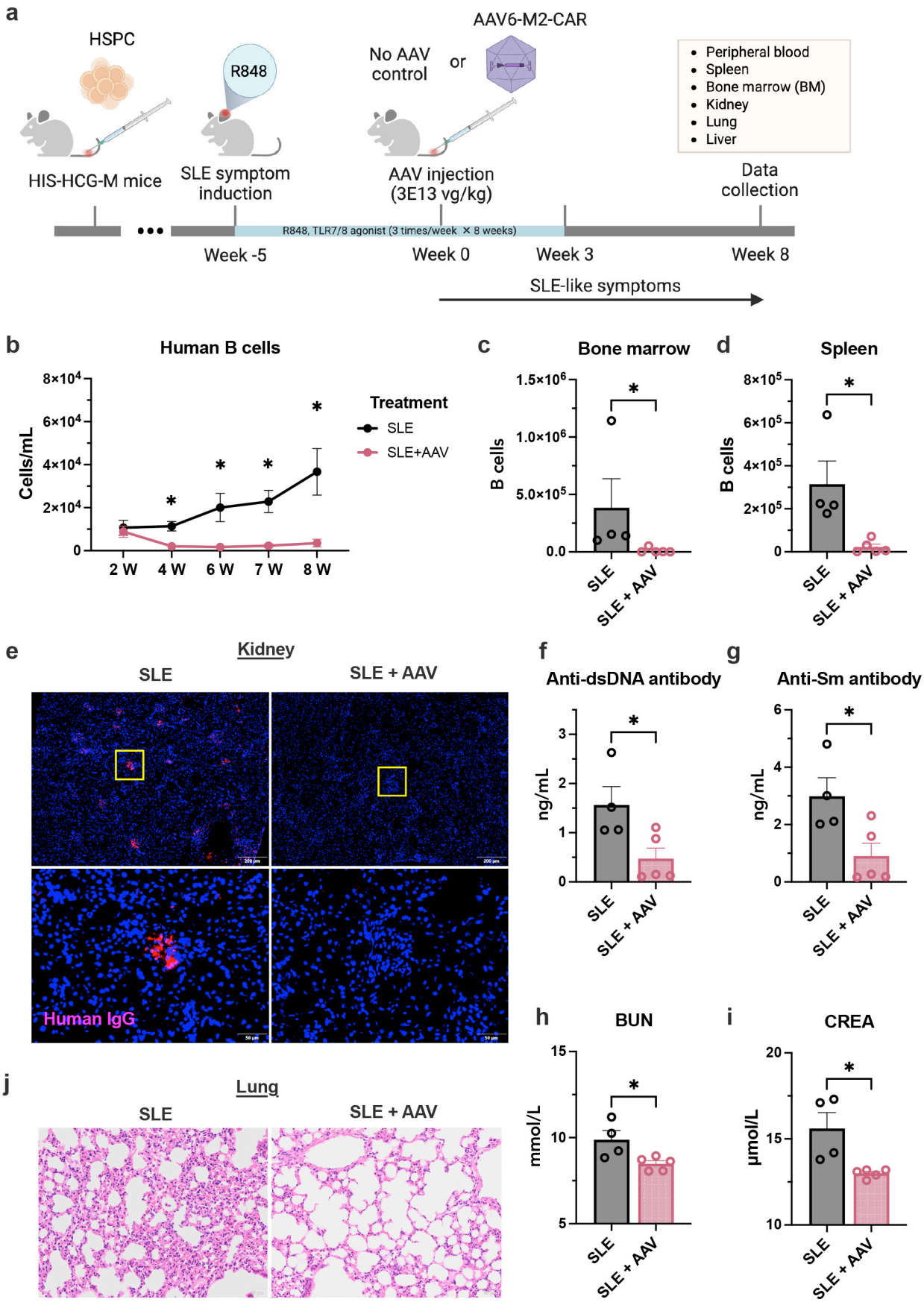

Fig. 5 AAV6-M2 *in vivo* CAR-T therapy eliminates B cells and ameliorates SLE symptoms in a humanized lupus model. a Experimental design. Humanized HIS-HCG-M mice were treated with R848 to induce SLE-like symptoms and injected with AAV6-M2-CAR. Tissues were collected at 8 weeks post-injection. **b** Quantification of human B cells in peripheral blood over time. **c**, **d** Total B cell counts in bone marrow (**c**) and spleen (**d**). **e** Representative kidney immunofluorescence images showing human IgG deposition (pink) in the SLE and SLE+AAV groups. Lower panels provide magnified views of the regions outlined by yellow rectangles in the corresponding upper panels. **f**, **g** Serum levels of anti-dsDNA (**f**) and anti-Smith (Sm) autoantibodies (**g**). **h**, **i** Levels of kidney injury markers BUN (**h**) and CREA (**i**). **j** Representative lung histology showing alveolar inflammation in SLE and its reduction upon AAV6-M2 treatment. Each dot represents an animal. Data shown as mean ± SEM. *P* values were calculated by unpaired *t*-tests. $^{*}P \le 0.05$; $^{**}P \le 0.01$; $^{***}P \le 0.001$; $^{****}P \le 0.0001$. ns: not significant.

Therefore, achieving both liver detargeting and T cell specificity is critical to bringing AAV into the realm of *in vivo* CAR-T therapy. By changing amino acids in the VR VIII loop, which protrudes to the surface of the AAV viral particle, AAV6-M2 exhibited strong tropism to human T cells while largely escaping from the liver. CRISPR-based receptor screening and validation confirmed that CD62L is required for AAV6-M2 transducing T cells, even without prior activation. The CD62L surface marker decorated naïve and early-memory T cells with higher plasticity and greater ability to proliferate, which are favored by CAR-T cell therapy. A higher viral copy number of AAV6-M2 in $CD62L^+$ T cells than that in $CD62L^-$ T cells in the spleen of HIS mouse provides preliminary in vivo evidence of CD62L preference (Supplementary Fig. S6a).

The interaction between the engineered VR VIII loop of AAV6-M2 and the EGF domain of CD62L was further supported by cryo-EM structural analysis and molecular docking. However, this does not explain why AAV6-M2 exhibits reduced liver uptake, where the liver sinusoidal endothelial cells (LSECs) and Kupffer cells are known to non-specifically sequester AAV particles from circulation. Notably, the engineered AAV6-M2 introduces three consecutive glutamic acids (E) to the VR VIII loop. These residues not only facilitate docking into a positively charged pocket in the EGF domain of CD62L, but also alter the capsid's surface electrostatic potential by contributing an additional ~120 negatively-charged amino acids (Supplementary Fig. S6b).

Indeed, the net loss of positive charge for AAV does alter the electrostatic properties of capsids, likely modulating its interactions with cellular receptors, antibodies, and other serum proteins[26]. Because circulating AAV particles can access the space of Disse, the increased negative surface charge of AAV6-M2 may reduce nonspecific interactions with the negatively-charged extracellular matrix, thereby potentially contributing to reduced hepatic AAV accumulation. Similar principles have been observed for LNP, where increasing negative surface charge can reduce hepatic sequestration and shift biodistribution toward the spleen, primarily by weakening nonspecific electrostatic interactions in the plasma and liver[27,28]. Consistent with this notion, a preliminary comparison of AAV6-M2 with Ark312 and Ark315, two AAV6 variants also engineered for human T cell targeting[29,30], suggests that AAV6-M2 exhibits lower liver accumulation relative to these variants (Supplementary Fig. S6c–e). Together, these observations raise the possibility that an increased number of negative surface charges may contribute to reduced hepatic viral genome levels; however, further investigation will be required to elucidate the mechanisms underlying liver detargeting and to inform future capsid engineering efforts.

Similar to the LNP, LV, and VLP platforms, our AAV-based *in vivo* CAR-T system demonstrates proof-of-concept but still requires further optimization through future biotechnological advancements. First, CAR sequences delivered as episomal DNA are subject to dilution as T cells proliferate. Although robust CAR-T cell signals were detected six weeks after AAV injection, site-specific CAR integration into the T cell genome using CRISPR may further extend CAR expression and provide more durable immune surveillance against target cells. Dual-AAV delivery represents a potential strategy to balance the need for stable CAR expression with the risks associated with random integration from lentiviral vectors. The differing kinetics of CAR-T cells generated via LNP, AAV, or lentiviral approaches warrant detailed investigation, as they likely dictate the most appropriate therapeutic indications for each platform. For example, a single dose of our current AAV-based *in vivo* CAR-T was sufficient to clear human B cells and ameliorate lupus-like pathology in HIS mice, whereas more persistent CAR-T cells may be required to control tumor progression. Second, leveraging AAV as a delivery platform to treat non-rare diseases, particularly tumors prone to relapse, offers exciting opportunities while also revisiting the long-standing challenge of redosing. LNP has been dosed repeatedly within a short interval (e.g., one week), boosting peripheral CAR-T cell levels[9]. Encouragingly, anti-CD40-mAb and CD20×CD3 bispecific antibodies have been used in non-human primates to suppress anti-AAV antibody response and enable repeat administration[31]. IgG degrading enzymes (e.g., Imlifidase) have also been actively investigated in preclinical and clinical studies for prophylactic immunomodulation in *in vivo* gene therapy, enabling AAV administration in the presence of pre-existing antibodies or allowing for re-administration in non-human primates[32]. Whether such strategies can similarly enhance the antigen-dependent cytotoxicity of AAV-delivered CAR-T cells remains a promising direction for future investigation. Finally, the use of T-cell-specific, compact, and potent promoters and enhancers may further enhance selective and robust CAR expression in the desired cell types, thereby increasing the safety margin.

We demonstrate that an engineered AAV6 variant, exhibiting superior transduction efficiency in human T cells and markedly reduced liver targeting, can deliver CAR sequences via systematic administration and generate functional CAR-T cells *in vivo*. This study establishes a novel *in vivo* CAR-T platform built upon a clinically validated and widely used delivery vector. Moreover, it broadens the therapeutic potential of AAV-mediated gene transfer beyond inherited disorders, extending into the treatment of acquired and immune-related diseases.

MATERIALS AND METHODS

AAV packaging

An ITR-containing GOI plasmid was utilized for packaging with different AAV capsid plasmids and adenovirus helper plasmid using polyethyleneimine (24765-1, Polysciences). To pack AAV, HEK 293T cells were seeded in 150 mm plates; The GOI, capsid, and helper plasmids were added at a ratio = 1:1:1 (Supplementary Table S1). After 72 h, the transfected HEK 293T cells were collected in SAN digestion buffer and lysed by three rounds of rapid freeze/thawing, followed by a 1 h incubation at 37 °C with 100 units/mL Benzonase (Yeasen, #20156E S60). AAV was further purified following cell harvest and PEG precipitation using iodixanol (StemCell Technologies, OptiPrep, #07820) gradient ultracentrifugation. The purified AAV was treated with DNaseI (Invitrogen, #AM2238) and Proteinase K (Qiagen, #W0013). The titer of AAV was determined by qPCR with ChamQ Universal SYBR qPCR Master Mix (Vazyme, #Q711) via LightCycler® 96 (Roche). Relative quantity was estimated compared to a serial dilution of a plasmid standard of known concentration. Primers for AAV titration were listed in Supplementary Table S2.

For large-scale AAV preparation, AAV particles were produced in a 3-liter bioreactor (Duoning) using WayneLVPro™ HEK293 cells (QUACELL) transfected with a three-plasmid system at a 1:1:1 ratio (GOI: capsid: helper plasmid). At 72 h post-transfection, cells were harvested, and

the AAV particles were purified by iodixanol gradient ultracentrifugation, followed by concentration and buffer exchange using tangential flow filtration. Final AAV products were resuspended in DPBS and stored at −80 °C.

The quality of purified AAV was assessed through: (1) Purity analysis by SDS-PAGE (SurePAGE, 4–20%, GenScript) with Coomassie Blue staining (GenScript); (2) Genomic titer quantification via absolute qPCR using ChamQ Universal SYBR qPCR Master Mix (Vazyme Q711) on a LightCycler® 96 System (Roche) was performed and titers were calculated from a standard curve generated by serial dilutions of linearized plasmid DNA containing the transgene expression cassette (concentration verified by Nanodrop™); (3) Ratio of full/empty capsid was determined by analytical ultracentrifugation (Beckman Optima AUC A/I, An-50 Ti rotor, 20 °C, 16,000 rpm).

Five GOIs were used in this study:
scAAV-EGFP: CAG-EGFP
ssAAV-Cas12f-sgRNA-EGFP: U6-sgRNA-CMV-Cas12f-EGFP
ssAAV-HDR-CD19CAR-EGFP: EF-1α-CD19CAR-TagBFP
ssAAV-CD19CAR-EGFP: EF-1α-CD19CAR-EGFP[33]
scAAV-EGFP-Barcode: CAG-EGFP-barcode

In vitro culture and transduction of primary cells and cell lines

• *Human PBMCs and primary T cells*

Peripheral blood from healthy donors was obtained with informed consent and institutional ethical approval (Westlake University, #20240318MLJ001) from Liquan Hospital (Shanghai, China), Boren Hospital (Beijing, China), and the Affiliated People's Hospital of Ningbo University (Ningbo, China).

PBMCs were isolated by density gradient centrifugation using Ficoll-Paque. Human primary T cells were subsequently purified from PBMCs using the Pan T Cell Isolation Kit (Miltenyi Biotec, #130-096-535) according to the manufacturer's instructions.

To conduct transduction in activated T cells, human T cells were activated using Enceed™ T cell Activation reagent (L00899, Genescript) for 24h in RPMI 1640 supplemented with 10% FBS and IL-2 at 100 U/mL (Jiangsu Kingsley Pharmaceutical Co., Ltd.). AAV vectors were then added at the indicated MOIs. Cells were maintained in IL-2-containing medium (100 U/mL) throughout the culture period.

To conduct transduction in cells without activation, human PBMCs and resting T cells were cultured in RPMI 1640 medium supplemented with 10% FBS, human IL-7 (5 ng/mL), and IL-15 (100 U/mL). Throughout the culture period, the medium was half changed every three days. To assess transduction efficiency in post-transduction activated T cells, activated human T cells were cultured in RPMI 1640 with 10% FBS and human IL-2 (100 U/mL) following activation. Cells were washed three times thoroughly at designated time points to remove residual AAV.

EGFP or CAR expression was assessed by flow cytometry at designated time points following AAV transduction. CAR expression was detected by Biotin-SP–Goat Anti-Mouse IgG, $F(ab')_2$ fragment-specific antibody (Jackson ImmunoResearch, #115-065-006), followed by PE-conjugated anti-biotin antibody (BioLegend, #409003).

• *Jurkat cells*

The Jurkat cells were purchased from ATCC (TIB-152) and cultured in RPMI1640 medium with 10% FBS. To generate Jurkat-SpCas9 cells, parental Jurkat cells were transduced with the LentiCas9-Blast vector (Addgene, #52962) and selected with 2 μg/mL blasticidin. Monoclonal SpCas9-expressing lines were established by limited dilution and expanded under continuous 0.5 μg/mL blasticidin selection.

• *NALM6 cells*

The NALM6 cell line was kindly provided by Dr. Xv Li's laboratory at Westlake University and maintained in RPMI 1640 medium with 10% FBS.

Cytotoxicity assay of CAR-T cells

To evaluate CAR-T cytotoxicity, activated human T cells were transduced with AAV6-WT-CAR or AAV6-M2-CAR at an MOI of 1×10^4. At day 2 post-transduction, NALM6 cells were co-cultured with transduced T cells at a 1:1 ratio (T cell:B cell, T:B). After 24 h of co-culture, cells were harvested and stained with anti-human CD45 and anti-human CD19 antibodies to distinguish NALM6 cells from human T cells. Cytotoxicity was calculated using the following formula:

Cytotoxicity (%) = 100 × ($CD19^+$% in non-AAV control − $CD19^+$% in AAV-transduced cells) / $CD19^+$% in non-AAV control.

To evaluate CAR-T cytotoxicity in resting human T cell subtypes, Central memory T cells (TCM; $CCR7^+CD45RO^+$), effector memory T cells (TEM; $CCR7^-CD45RO^+$), and naïve T cells (TN; $CCR7^+CD45RO^-$) were isolated from pre-cultured human T cells using fluorescence-activated cell sorter (BD FACSAria Fusion) and maintained in RPMI 1640 medium supplemented with 10% FBS, IL-7 (5 ng/mL), and IL-15 (100 U/mL). Each subset was transduced with recombinant AAV (AAV) at an MOI of 1×10^5. At 24 h post-transduction, cells were washed three times with RPMI 1640 and co-cultured with NALM6 cells at a T:B ratio of 3:1. From that point forward, the percentages of NALM6 cell ($CD45^-CD19^+$), TCM, TEM, Tn, and TEMRA ($CCR7^-CD45RO^-$) populations in each well were assessed by flow cytometry every three days.

Serum blocking assay

Serum samples were collected from 36 healthy donors at Zhejiang Cancer Hospital. All procedures, including serum collection and experimental assays, were conducted under ethical approval from both Zhejiang Cancer Hospital and Westlake University (#20250527MLJ001). PBMC from four donors were used in this experiment.

To assess the inhibition of AAV transduction by pre-existing neutralizing antibodies, serial 10-fold dilutions of human serum (prepared in RPMI 1640 supplemented with 2% FBS, starting at 1:2.5) were prepared in an 8-tube strip and mixed with equal volumes of AAV6-M2-EGFP or AAV6-WT-EGFP (diluted in RPMI 1640 + 2% FBS) in a U-bottom 96-well plate. The virus-serum mixtures were incubated at 37 °C with 5% CO_2 for 1 h, resulting in final serum dilutions ranging from 1:5 to 1:5,000 across four serial dilution steps.

After incubation, 5×10^4 human PBMCs, pre-activated via Enceed™ T cell Activation reagent (Genescript, #L00899) and human IL-2 for 24 h, were added to each well. Each well contained a final volume of 200 μL RPMI 1640 with 2% FBS and 100 U/mL IL-2. AAVs were added at an MOI of 5×10^3. Positive control wells contained AAV without serum, and negative control wells contained neither AAV nor serum.

At 48 h post-transduction, cells were stained with anti-

human CD45 (BioLegend, #304012) and anti-human CD3 (BioLegend, #317308), and EGFP expression in $CD3^+CD45^+$ T cells was analyzed by flow cytometry. The $EGFP^+$ percentage was normalized using the formula:

(Sample EGFP% − Negative Control EGFP%) / (Positive Control EGFP% − Negative Control EGFP%) × 100%.

Donors were grouped based on the highest dilution factor at which the $EGFP^+$ percentage dropped below 50%, and the number of donors in each group was plotted for AAV6-WT and AAV6-M2, respectively.

Site-specific CAR insertion

The first AAV vector packaged sequences that encode CD19 CAR linked to tagBFP, with the two expression cassettes connected by a self-cleaving T2A sequence. The CD19 CAR cassette was flanked by two 400-bp homology arms corresponding to the insertion sites generated by a CRISPR system delivered by the second AAV. The second AAV vector packaged sequences encoding an engineered AsCas12f-HKRA (enAsCas12f-HKRA), a nuclear localization signal, EGFP, T2A, and an sgRNA targeting the first exon of *TRAC*.

The dual AAV vectors were co-transduced into activated human T cells at an MOI 1×10^5. Transduced cells were cultured in RPMI 1640 medium supplemented with 10% FBS and 100 U/mL IL-2. The percentages of GFP^+ and BFP^+ cells were monitored by flow cytometry post-transduction. Cells were also stained with anti-TCR α/β (Biolegend, #306727) to assess TCR knockout, and the CAR expression was evaluated by Biotin-SP–Goat Anti-Mouse IgG, $F(ab')_2$ fragment-specific antibody (Jackson ImmunoResearch, #115-065-006), followed by PE-conjugated anti-biotin antibody (BioLegend, #409003). Stable CAR^+ T cells were defined as TCR^-CAR^+ cells.

Genomic insertion of the CAR sequence was verified by PCR amplifying the flanking regions surrounding the insertion sites.

Genome-wide CRISPR-Cas9 screening

• Preparing the LV Brunello library

The transfer plasmid (LentiGuide-Brunello-mKate2), the pMD2.G (Addgene, #12259) envelope plasmid, and the psPAX2 (Addgene, #12260) packaging plasmid were mixed at the mass ratio 5:2:3 and incubated with PEI for 15 min at room temperature. The mixture was dropped to HEK293T cells at 80% confluency. Lentiviral supernatant was collected at 48 and 72 h post-transfection, filtered through a 0.45-μm filter (Millipore, #SLHV033RB), and then concentrated by ultracentrifuging at 70,000× *g* at 4 °C for 2 h. Finally, the concentrated LV was aliquoted and stored at −80°C.

• CRISPR-Cas9 screening in Jurkat-Cas9 cells

LentiGuide-Brunello-mKate2 was transduced in Jurkat with stable Cas9 expression (Jurkat-Cas9). The screening was performed in two Jurkat-Cas9 mono clones. For each replicate, 7×10^7 Cas9-expressing Jurkat cells (~300X coverage) were transduced with the lentiviral library at MOI ≤ 0.3 by infection and incubated overnight. Flow cytometry confirmed transduction efficiencies at around 30% in each replicate for $mKate2^+$% expression at 72 h after LV transduction. Cas9-expressing Jurkat cells (Jurkat-Cas9) were selected and expanded in a culture medium with puromycin. When $mKate2^+$% achieved above 95%, 1×10^7 cells per replicate were transduced with AAV6-WT-EGFP or AAV-M-EGFP at the indicated MOI to allow the percentage of $EGFP^+$ cells to reach over 80%. At 72 h after AAV transduction, cells collected for the top 20% and bottom 20% were sorted via Flow Cytometer. BD FACSAria™ Fusion and SONY MA900 were used for cell sorting.

After sorting, genomic DNA was extracted by TIANamp Genomic DNA Kit (TIANGEN, DP304-03). Then, sgRNA sequences were amplified using Q5 master mix (2×) (NEB, #M0544S) and purified using SPRI beads (Beckman, #A63882) for NGS. PCR primers with P5 and P7 adapters (NGS-Lib-KO-F and NGS-Lib-KO-R) were listed in Supplementary Table S2. sgRNA sequences used in validation were listed in Supplementary Table S3.

• Screening data analysis

The CRISPR screening was analyzed using MAGeCK[34]. The difference in genes between the bottom 20% of cells and the top 20% of cells was evaluated by the read count of corresponding gRNAs. In addition, the negative gRNAs were input as background with the parameter (--control-sgrna). The MAGeCK score and $\log_2$ fold change were used to rank genes from the CRISPR screening. The $\log_2$ fold change was calculated as the $\log_2$ transformed ratio between the normalized read counts in the bottom 20% sample and the top 20% sample. Normalization was based on the sequencing depth of each sample.

• Validating candidate genes in Jurkat cells

Candidate gene-knockout cell lines were generated using Jurkat-Cas9 cells transduced with LV encoding the indicated sgRNA under the U6 promoter. From day 2 after LV transduction, Jurkat cells were selected with puromycin (2 μg/mL) for 7–10 days. Then, the genomic DNA of the Jurkat cells was extracted for PCR amplification of the target gene sequence. The indel% of the target gene was assessed via SYNTEGO analysis based on Sanger sequencing of PCR products. Primers used in Sanger sequencing for knock-out validation were listed in Supplementary Table S2. Before AAV transduction, $CD62L^-$ cells were sorted via BD FACSAria™ Fusion for high purity. For each group, a total of 5×10^4 Jurkat cells were transduced with AAV6-WT-EGFP or AAV6-M2-EGFP. 48 h after AAV transduction, cells were collected and tested for EGFP expression via flow cytometry.

• Validating candidate genes in human T cells

Following 24 h of activation, human T cells were nucleofected using the P3 Primary Cell 4D-Nucleofector™ X Kit (Lonza, #V4XP-3032) and a 4D-Nucleofector™ X Unit (Lonza, #AAF-1003X). SgRNAs were synthesized by GenScript (Supplementary Table S3). RNP complexes were prepared by incubating 30 pmol of recombinant Cas9 protein (Takara, #632641) with 75 pmol of sgRNA at 25 °C for 10 min. A total of 1×10^6 activated T cells were electroporated with RNPs per well using the EO-115 program. After nucleofection, cells were resuspended in fresh culture medium supplemented with cytokines. Three days post-knockout, AAV6-WT-EGFP or AAV6-M2-EGFP were added to the culture at an MOI of 1×10^4. Another three days later (day 6 post-nucleofection), cells were collected and stained with anti-CD62L antibody. EGFP expression was analyzed by flow cytometry in both $CD62L^+$ and $CD62L^-$ T cell populations.

Cryo-EM structure

For cryo-EM sample preparation, 3.5 μL of the AAV sample

(1.3×10^{14} vg/mL) was applied to a glow-discharged Quantifoil R1.2/1.3 Cu 300 mesh grid. Grids were blotted for 4 s with a blot force of 10 following a 6 s waiting time using a Vitrobot Mark IV (Thermo Fisher Scientific) under 100% humidity at 4 °C. The grids were then plunge-frozen in liquid ethane cooled by liquid nitrogen.

Data collection was performed on a Titan Krios transmission electron microscope (Thermo Fisher Scientific) operating at 300 kV, equipped with a Gatan K3 Summit direct electron detector and a GIF Quantum energy filter (20 eV slit width). Movie stacks were recorded in super-resolution mode at a nominal magnification of 130,000× using EPU software, with a preset defocus range of −1.4 to −2.0 µm in Aberration-Free Image Shift (AFIS) mode. Each stack was exposed for 0.85 s (32 frames, 0.0266 s per frame), with a total electron dose of ~50 $e^-/Å^2$.

A total of 11,707 movie stacks were collected. Of these, 9,621 micrographs were manually selected and processed using CryoSPARC v4.6.2. Patch motion correction and Patch CTF estimation were applied. An initial round of auto-picking yielded ~157,325 particles with a box size of 640 pixels. After iterative rounds of template-based particle picking and 2D classification, 156,281 particles were selected for *ab initio* reconstruction (C1 symmetry). Homogeneous refinement, followed by local CTF refinement and non-uniform refinement, produced a final 3D reconstruction at an overall resolution of 1.8 Å.

A structural model of AAV6-M2 was initially generated using the AlphaFold3 prediction[35]. Manual model adjustment and refinement were performed in COOT[36], followed by atomic-level refinement using Phenix[37]. Structural figures were prepared using ChimeraX[38].

Receptor docking

Flexible docking between AAV6-M2 and the transmembrane receptor L-selectin was performed using the HADDOCK2.4 web server[39]. The input structures included the AAV6-M2 trimer (PDB: 9VI4) and the lectin/EGF domains of L-selectin (PDB: 5VC1). All small molecules were removed from the L-selectin structure, except for the calcium ion. The engineered loop region of one AAV6-M2 monomer and the EGF domain of L-selectin were defined as active residues for docking. The top-ranked docking model was visualized using ChimeraX[38].

Mouse experiments

• *HIS mice generation*

NOD/ShiLtJGpt-Prkdc^{em26Cd52}Il2rg^{em26Cd22}kit$^{em1Cin(V831M)}$Il15$^{em1Cin(hIL15)}$/Gpt (NCG-X-hIL15) mice (Strain NO. T037155) and NOD/ShiLtJGpt-Prkdc^{em26Cd52} Il2rg^{em26Cd22} Rosa26$^{em1Cin(hCSF2\&IL3\&KITLG)}$/Gpt (NCG-M) mice (Strain NO. T036669) were purchased from GemPharmatech Co., Nanjing, China. These mice were housed under specific pathogen-free conditions at the Model Animal Research Center, Medical School of Nanjing University, with all experiments conducted in compliance with institutional guidelines under an approved animal protocol (LY-02). HIS mice were generated as previously described[40]. Briefly, human hematopoietic stem and progenitor cells (HSPCs) were purified from fetal liver using the human CD34 MicroBead Kit (Miltenyi Biotec, #130-046-702) following ethical approval (Drum Tower Hospital, protocol #2021-488-01/02). Newborn NCG-M mice received 80 cGy sublethal irradiation followed by intrahepatic injection of 5×10^4 $CD34^+CD38^-$ HSCs within 4–6 days after birth, whereas non-irradiated NCG-X-hIL15 mice underwent the same HSC transplantation procedure. Successful immune reconstitution was confirmed at 10 weeks post-engraftment by flow cytometry detection of human immune cells ($CD45^+$, $CD3^+$, $CD19^+$, $CD14^+$, $CD56^+$) in peripheral blood, with engraftment defined as > 1×10^5 human $CD45^+$ cells/mL.

• *In vivo CAR-T generation in HIS mice*

Humanized NCG-X-hIL15 mice demonstrating sufficient T cell engraftment (≥ 15% human $CD3^+$ T cells in peripheral blood human $CD45^+$ cells) were randomly assigned to two experimental groups. These groups received intravenous administration of either AAV-M2-CAR19-EGFP or AAV6-CAR19-EGFP at a dose of 3×10^{13} vg/kg. Peripheral blood CART signal and B cell dynamics were monitored at bi-weekly intervals via flow cytometry. Mice were sacrificed 4 weeks and 6 weeks post-AAV injection for comparative immune cells profiling in indicated tissues, including CAR-T cell transduction efficiency ($EGFP^+$ in human $CD3^+$ T cells, $CD4^+$ T cells, $CD8^+$ T cells, Tn cells, TCM cells, TEM cells, TEMRA cells) and B cell depletion. Flow cytometry (Agilent NovoCyte Penteon, Santa Clara, USA) was used for cell population detection. Antibodies were listed in Supplementary Table S4. Gating strategies were summarized in Supplementary Fig. S7a.

• *Evaluation of lupus pathologies in AAV6-M2-CD19CAR-treated HIS SLE mice*

HIS-SLE mouse model was generated as previously described[41]. Briefly, we topically administered the TLR7/8 agonist R848 to NCG-M HIS mice for eight consecutive weeks to induce systemic lupus-like manifestations. Following five weeks of R848 treatment, mice demonstrated comparable levels of human immune reconstitution (quantified by peripheral blood human $CD45^+$ cell counts) and elevated serum autoantibody titers (quantified by anti-dsDNA antibody) were randomly allocated to receive either AAV6-M2-CD19CAR (3×10^{13} vg/kg, i.v.) or PBS control. Mice were euthanized at 8 weeks post-AAV administration for endpoint analysis. Then, serum autoantibody levels were measured by ELISA: anti-dsDNA antibody (COIBO BIO, #CB13357-Hu) and anti-Sm antibody (COIBO BIO, #CB19966-Hu) following the manufacturer's instructions. Serum biochemical profiling was quantified using an automated clinical analyzer (HITACHI 3500, Tokyo, Japan) following manufacturer-recommended protocols. Subsequently, B cell subsets (Transitional B, Naïve B, Plasmablast, Memory B) in indicated tissues were further analyzed by flow cytometry. All antibodies used were listed in Supplementary Table S4. Gating strategies were summarized in Supplementary Fig. S7b.

• *Quantification of AAV accumulation in the liver of HIS mice*

Various organs from HIS mice were collected at the endpoint of the experiment. For each organ, a 50–80 mg minced tissue sample was homogenized, and genomic DNA was extracted using the TIANamp Genomic DNA Kit (TIANGEN, #DP304-03). Absolute quantification of AAV-delivered CAR copies was performed via qPCR using 100 ng of gDNA per reaction. Primers (QCAR-F, QCAR-R) and probes (QCAR-Probe) targeting the CAR transgene were designed as listed in Supplementary Table S2. PCR amplification was conducted using Hot Start Taq 2× Master Mix (NEB, #M0496S) with the following thermocycling conditions: 95 °C for 30 s, followed by 40 cycles of 95 °C for 15 s, 52 °C for 30 s, and 68 °C for 20 s. Ct

values were converted to AAV vector genome copies (Vg) based on a standard curve.

• ***Quantification of AAV accumulation in human T cell subpopulation in the spleen of HIS mice***

Humanized NCG-X-hIL15 mice received intravenous administration of AAV6-M2-CAR19-EGFP at a dose of 3×10^{13} vg/kg. Mice were sacrificed at 12 h post AAV injection, and spleen was taken for cell sorting. Four cell populations, including human $CD4^+CD62L^+$ cells, human $CD4^+CD62L^-$ cells, human $CD8^+CD62L^+$ cells, human $CD8^+CD62L^-$ cells were sorted for $1\sim2 \times 10^5$. Then, the genomic DNA of each cell population was extracted by DNeasy Blood & Tissue Kit (Qiagen, 69504). Absolute quantifications of AAV6-M2-CAR19-EGFP copies and human beta-actin copies were performed via qPCR using 30 ng of gDNA per reaction. PCR amplification was conducted using Hot Start Taq 2× Master Mix with the following thermocycling conditions: 95 °C for 30 s, followed by 40 cycles of 95 °C for 15s, 52 °C for 30 s, and 68 °C for 20 s. Ct values were converted to AAV vector genome copies (Vg) based on a standard curve.

• ***Quantification of AAV accumulation in the liver of B6 mice***

C57BL/6J mice were purchased from the Animal Center of Westlake University and housed under standard, individually ventilated, pathogen-free conditions at the Laboratory Animal Resource Center of Westlake University. All animal experiments were conducted in accordance with the Institutional Animal Care and Use Committee (IACUC) guidelines approved by Westlake University. Six-week-old mice were administered scAAV6-WT-EGFP, scAAV6-M2-EGFP, scAAV6-Ark312-EGFP, or scAAV6-Ark315-EGFP via intravenous injection at a dose of 5×10^{12} vg/kg. Phosphate-buffered saline (PBS) was injected intravenously as a negative control. At day 10 post-injection, mice were euthanized, and livers were harvested for EGFP expression analysis using the PHOTON IMAGER™ OPTIMA system, and EGFP signals from individual livers were quantified. The AAV viral copies in the liver were also quantified by qPCR using a similar approach as described in the HIS mice section. The capsid sequences of Ark312 and Ark315 were obtained from published patents[29,30].

H&E staining

Liver and lung tissues were fixed in 4% paraformaldehyde (Beyotime Biotechnology, P0099) at room temperature for 24 h, dehydrated through a graded ethanol series, cleared in xylene, and embedded in paraffin. Tissue sections were cut using a microtome, mounted on glass slides, and dried overnight. H&E staining, sections were deparaffinized in xylene, rehydrated through a descending ethanol series (100% to 70%), stained with Harris' hematoxylin for 3 min, and counterstained with eosin Y for 1 min. Slides were then dehydrated through an ascending ethanol series, cleared in xylene, and coverslipped. Stained sections were examined using an Olympus microscope (VS200, Olympus, Tokyo, Japan).

Cynomolgus macaque experiments

The non-human primate (NHP) experiments were conducted at the NHP facility of Innostar Biotechnology and approved by Innostar's Institutional Animal Care and Use Committee (IACUC). A 2-year-old cynomolgus macaque was used in this study. Four weeks after intravenous administration of AAV (1×10^{12} vg/kg), the animal was euthanized with 10 mg/kg ketamine hydrochloride and 5 mg/kg xylazine hydrochloride, followed by PBS perfusion. To quantify viral genome copies, 50–100 mg of tissue samples were homogenized in Buffer ATL (QIAGEN) using a tissue grinder. Genomic DNA and viral DNA were extracted using the DNeasy Blood & Tissue Kit (QIAGEN) according to the manufacturer's instructions. Vector genomes were amplified from the extracted DNA using primers flanking the transgene and the Q5 High-Fidelity Master Mix (NEB, #M0544S). Amplicons containing Illumina adapter sequences were quantified using Qubit, pooled at equal mass, and sequenced on an Illumina NovaSeq X Plus platform.

Flow cytometry data collection and analysis

Flow cytometry (Agilent NovoCyte Penteon and CytoFLEX) was used to analyze cells. Flow cytometry data were analyzed via FlowJo.

Statistical analysis

Statistical analysis was performed using GraphPad Prism v10, and the specific tests were indicated in the figure legend.

ACKNOWLEDGMENTS

We thank the Biomedical Research Core Facilities, Laboratory Animal Resource Center, and High-Performance Computer Center of Westlake University for their excellent technical assistance. This work was supported by grants from the National Science Foundation of China (32471533, 32471000, U24A20378), the National Science and Technology Major Program (2025ZD01900700, 2023ZD0500400), the Pioneer and Leading Goose R&D Program of Zhejiang (2024SSY0003), the Fundamental Research Funds for the Central Universities (XJ2024003602, 0214-14380533), and the Research Center for Industries of the Future (RCIF) at Westlake University. This work was also partially supported by Westlake Genetech Inc. and Changping Laboratory.

AUTHOR CONTRIBUTIONS

L.M., Y.L., and Z.L. conceived the project and designed the experiments. L.M. and Z.L. designed the capsid library. Y.L. designed the HIS mouse model. Q.S. and J.Wang conducted AAV library preparation and screening with the help of J.Wu and Y.X. K.N. and W.L. conducted CAR-T experiments *in vitro* and *in vivo*, receptor CRISPR screening and validation with help from M.W., L.W., C.W., Y.C., R.Z., S.D., C.C., B.K., S.W., and X.Q. Y.Z. and X.W. conducted cryo-EM experiments with guidance from Y.W. R.D. prepared AAV with help from the Westlake Genetech CMC team. Z.L., R.Z., and H.C. conducted computational analysis and molecular docking analysis with the help of Q.Z. G.W., L.M., Z.L., K.N., Y.L., and W.L. wrote the manuscript with input from all co-authors.

COMPETING INTERESTS

Westlake Genetech and Westlake University share intellectual property based on the AAV variants of this study. Z.L. and L.M. are co-founders of Westlake Genetech. K.N. was a postdoc in Lijia Ma's Lab at Westlake University when this project started. K.N., M.W., L.W., Q.Z., J.W., B.K., Y.X., S.W., G.W., R.D., and H.C. are currently full-time employees of Westlake Genetech. Y.L. is currently consulting for GemPharmatech Co.

REFERENCES

1. Baker, D.J., Arany, Z., Baur, J.A., Epstein, J.A. & June, C.H. CAR T therapy

beyond cancer: the evolution of a living drug. *Nature* **619**, 707–715 (2023).
2. Maus, M.V. A decade of CAR T cell evolution. *Nat. Cancer* **3**, 270–271 (2022).
3. Depil, S., Duchateau, P., Grupp, S.A., Mufti, G. & Poirot, L. 'Off-the-shelf' allogeneic CAR T cells: development and challenges. *Nat. Rev. Drug Discov.* **19**, 185–199 (2020).
4. Short, L., Holt, R.A., Cullis, P.R. & Evgin, L. Direct in vivo CAR T cell engineering. *Trends Pharmacol. Sci.* **45**, 406–418 (2024).
5. Rurik, J.G. et al. CAR T cells produced in vivo to treat cardiac injury. *Science* **375**, 91–96 (2022).
6. Thomsen, G. et al. Biodistribution of onasemnogene abeparvovec DNA, mRNA and SMN protein in human tissue. *Nat. Med.* **27**, 1701–1711 (2021).
7. Kheirolomoom, A. et al. *In situ* T-cell transfection by anti-CD3-conjugated lipid nanoparticles leads to T-cell activation, migration, and phenotypic shift. *Biomaterials* **281**, 121339 (2022).
8. Billingsley, M.M. et al. *In vivo* mRNA CAR T cell engineering via targeted Ionizable lipid nanoparticles with extrahepatic tropismrahepatic tropism. *Small* **20**, 2304378 (2024).
9. Hunter, T.L. et al. *In vivo* CAR T cell generation to treat cancer and autoimmune disease. *Science* **388**, 1311–1317 (2025).
10. Michels, A. et al. Lentiviral and adeno-associated vectors efficiently transduce mouse T lymphocytes when targeted to murine CD8. *Mol. Ther. Methods Clin. Dev.* **23**, 334–347 (2021).
11. Pfeiffer, A. et al. *In vivo* generation of human CD19-CAR T cells results in B-cell depletion and signs of cytokine release syndrome. *EMBO Mol. Med.* **10**, e9158 (2018).
12. Charitidis, F.T., Adabi, E., Thalheimer, F.B., Clarke, C. & Buchholz, C.J. Monitoring CAR T cell generation with a CD8-targeted lentiviral vector by single-cell transcriptomics. *Mol. Ther. Methods Clin. Dev.* **23**, 359–369 (2021).
13. Frank, A.M. et al. Combining T-cell-specific activation and *in vivo* gene delivery through CD3-targeted lentiviral vectors. *Blood Adv.* **4**, 5702–5715 (2020).
14. Huckaby, J.T. et al. Bispecific binder redirected lentiviral vector enables *in vivo* engineering of CAR-T cells. *J. Immunother. Cancer* **9**, e002737 (2021).
15. Andorko, J.I. et al. Targeted *in vivo* delivery of genetic medicines utilizing an engineered lentiviral vector platform results in CAR T and NK cell generation. *Mol. Ther.* **33**, 4937–4952 (2025).
16. Xu, J. et al. *In-vivo* B-cell maturation antigen CAR T-cell therapy for relapsed or refractory multiple myeloma. *Lancet* **406**, 228–231 (2025).
17. Banskota, S. et al. Engineered virus-like particles for efficient *in vivo* delivery of therapeutic proteins. *Cell* **185**, 250–265.e16 (2022).
18. Hamilton, J.R. et al. Targeted delivery of CRISPR-Cas9 and transgenes enables complex immune cell engineering. *Cell Rep.* **35**, 109207 (2021).
19. Hamilton, J.R. et al. *In vivo* human T cell engineering with enveloped delivery vehicles. *Nat. Biotechnol.* **42**, 1684–1692 (2024).
20. Li, C.W. & Samulski, R.J. Engineering adeno-associated virus vectors for gene therapy. *Nat. Rev. Genet.* **21**, 255–272 (2020).
21. Nyberg, W.A. et al. An evolved AAV variant enables efficient genetic engineering of murine T cells. *Cell* **186**, 446–460.e19 (2023).
22. Nyberg, W.A. et al. *In vivo* engineering of murine T cells using the evolved adeno-associated virus variant Ark313. *Immunity* **58**, 499–512.e7 (2025).
23. Arbonés, M.L. et al. Lymphocyte homing and leukocyte rolling and migration are impaired in L-selectin-deficient mice. *Immunity* **1**, 247–260 (1994).
24. Dhungel, B.P., Bailey, C.G. & Rasko, J.E.J. Journey to the center of the cell: tracing the path of AAV transduction. *Trends Mol. Med.* **27**, 172–184 (2021).
25. Kapitza, L. et al. CD62L as target receptor for specific gene delivery into less differentiated human T lymphocytes. *Front. Immunol.* **14**, 1183698 (2023).
26. Hsu, H.L. et al. Structural characterization of a novel human adeno-associated virus capsid with neurotropic properties. *Nat. Commun.* **11**, 3279 (2020).
27. Cheng, Q. et al. Selective organ targeting (SORT) nanoparticles for tissue-specific mRNA delivery and CRISPR-Cas gene editing. *Nat. Nanotechnol.* **15**, 313–320 (2020).
28. Baek, M.J., Hur, W., Kashiwagi, S. & Choi, H.S. Design considerations for organ-selective nanoparticles. *ACS Nano* **19**, 14605–14626 (2025).
29. Eyquem, J. & Nyberg, W.A. *In vivo* modification of cell genomes. WO2025179057(A1) (2025).
30. Eyquem, J., Nyberg, W.A., Asokan, A. & Ark, J. Adeno-associated virus compositions and methods of use thereof for human cells. WO2025179007(A1) (2025).
31. Giovannone, N. et al. Successful AAV vector re-administration via two distinct B cell immunomodulation strategies in non-human primates. *Mol. Ther.* (2025).
32. Leborgne, C. et al. IgG-cleaving endopeptidase enables in vivo gene therapy in the presence of anti-AAV neutralizing antibodies. *Nat. Med.* **26**, 1096–1101 (2020).
33. Rodgers, D.T. et al. Switch-mediated activation and retargeting of CAR-T cells for B-cell malignancies. *Proc. Natl. Acad. Sci. USA* **113**, E459–E468 (2016).
34. Li, W. et al. MAGeCK enables robust identification of essential genes from genome-scale CRISPR/Cas9 knockout screens. *Genome Biol.* **15**, 554 (2014).
35. Abramson, J. et al. Accurate structure prediction of biomolecular interactions with AlphaFold 3. *Nature* **630**, 493–500 (2024).
36. Emsley, P., Lohkamp, B., Scott, W.G. & Cowtan, K. Features and development of *Coot*. *Acta Crystallogr. D Biol. Crystallogr.* **66**, 486–501 (2010).
37. Liebschner, D. et al. Macromolecular structure determination using X-rays, neutrons and electrons: recent developments in *Phenix*. *Acta Crystallogr. D Struct. Biol.* **75**, 861–877 (2019).
38. Pettersen, E.F. et al. UCSF ChimeraX: structure visualization for researchers, educators, and developers. *Protein Sci.* **30**, 70–82 (2021).
39. Honorato, R.V. et al. The HADDOCK2.4 web server for integrative modeling of biomolecular complexes. *Nat. Protoc.* **19**, 3219–3241 (2024).
40. Ren, D.S., Liu, W., Ding, S. & Li, Y. Protocol for generating human immune system mice and hydrodynamic injection to analyze human hematopoiesis in vivo. *STAR Protoc.* **3**, 101217 (2022).
41. Zhu, R.J. et al. An advanced humanized systemic lupus erythematosus model enables parallel profiling of B cell-targeted therapies. *bioRxiv* https://doi.org/10.64898/2026.01.27.701893 (2026).

ADDITIONAL INFORMATION

Supplementary information The online version contains supplementary material available at https://doi.org/10.15302/vita.2026.01.0008.

Correspondence and requests for materials should be addressed to Yan Li or Lijia Ma.